VIP Carbon Materials Very Important Paper

How to cite: *Angew. Chem. Int. Ed.* **2021**, *60*, 26115–26121
International Edition: doi.org/10.1002/anie.202109808
German Edition: doi.org/10.1002/ange.202109808

NBN-Doped *Bis*-Tetracene and *Peri*-Tetracene: Synthesis and Characterization

Yubin Fu[+], Xiao Chang[+], Huan Yang[+], Evgenia Dmitrieva, Yixuan Gao, Ji Ma, Li Huang, Junzhi Liu,* Hongliang Lu, Zhihai Cheng, Shixuan Du, Hong-Jun Gao, and Xinliang Feng**

Abstract: *Combining solution-based and surface-assisted synthesis, we demonstrate the first synthesis of NBN-doped bis-tetracene (**NBN-BT**) and peri-tetracene (**NBN-PT**). The chemical structures are clearly elucidated by high-resolution scanning tunneling microscopy (STM) in combination with noncontact atomic force microscopy (nc-AFM). Scanning tunneling spectroscopy (STS) characterizations reveal that **NBN-BT** and **NBN-PT** possess higher energy gaps than bis-tetracene and peri-tetracene. Interestingly, **NBN-BT** can undergo stepwise one-electron oxidation and convert into its corresponding radical cation and then to its dication. The energy gap of the **NBN-BT** dication is similar to that of bis-tetracene, indicating their isoelectronic relationship. Moreover, a similar energy gap between the **NBN-PT** dication and peri-tetracene can be predicted by DFT calculations. This work provides a novel synthesis along with characterizations of multi-NBN-doped zigzag-edged peri-acenes with tunable electronic properties.*

Acenes, which can be regarded as laterally fused benzene rings, have drawn great interest in recent decades.[1] From a structural point of view, acenes can be classified as a unique type of polycyclic aromatic hydrocarbon (PAH) with zigzag-edged peripheries (Figure 1 a).[1c,e] When two linear acenes are laterally fused at the *peri*-positions, the resultant PAHs are named *peri*-acenes.[2] Typical *peri*-acenes possess two armchair edges and extended zigzag-edged topologies (Figure 1 a).[2,3] As the precursors of *peri*-acenes, *bis*-acenes also possess extended zigzag-edged topologies (Figure 1 a).[4] The smaller *peri*-acenes, perylene, and *bis*-anthene, have been well

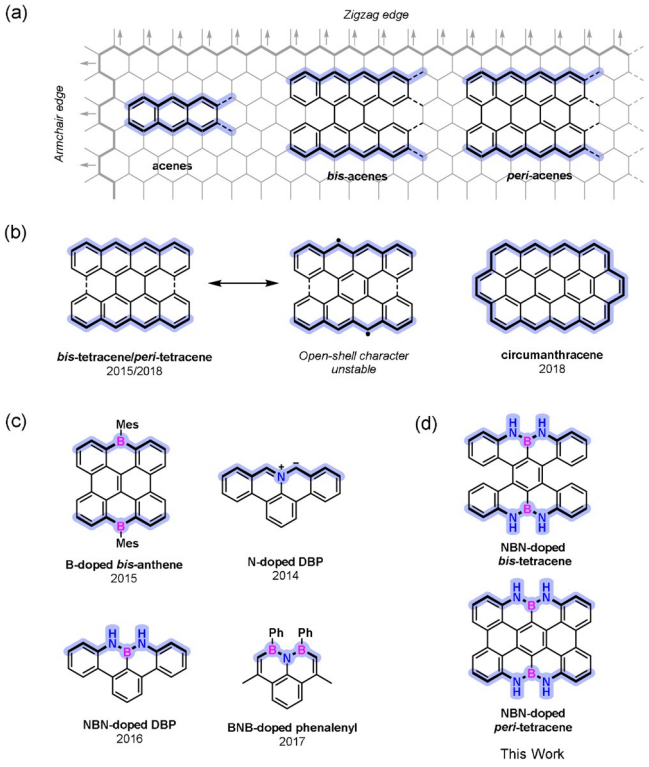

Figure 1. a) Chemical structures of acenes, *bis*-acenes, and *peri*-acenes; b) chemical structures of *bis*-tetracene, *peri*-tetracene, and circumanthracene; c) chemical structures of B-doped *bis*-anthene, N-doped dibenzophenalene (DBP), NBN-doped DBP, and BNB-doped phenalenyl; and d) this work: NBN-doped *bis*-tetracene (**NBN-BT**) and NBN-doped *peri*-tetracene (**NBN-PT**). The substituents of all structures are omitted for simplicity.

[*] Dr. Y. Fu,[+] Dr. J. Ma, Prof. X. Feng
Center for Advancing Electronics Dresden (cfaed) & Faculty of Chemistry and Food Chemistry, Technische Universität Dresden
01062 Dresden (Germany)
E-mail: xinliang.feng@tu-dresden.de

X. Chang,[+] Dr. H. Yang,[+] Y. Gao, Dr. L. Huang, Dr. H. Lu, Prof. S. Du, Prof. H. Gao
Institute of Physics and University of Chinese Academy of Sciences, Chinese Academy of Sciences
Beijing 100190 (China)
E-mail: lhuang@iphy.ac.cn

Dr. E. Dmitrieva
Leibniz Institute for Solid State and Materials Research
01069 Dresden (Germany)

Dr. J. Liu
Department of Chemistry and State Key Laboratory of Synthetic Chemistry, The University of Hong Kong
Pokfulam Road, Hong Kong (China)
E-mail: juliu@hku.hk

Dr. Z. Cheng
Department of Physics and Beijing Key Laboratory of Optoelectronic Functional Materials & Micro-nano Devices, Renmin University of China
Beijing 100872 (China)

[+] These authors contributed equally to this work.

Supporting information and the ORCID identification number(s) for the author(s) of this article can be found under: https://doi.org/10.1002/anie.202109808.

investigated for several decades.[5,6] Higher *peri*-acenes, from *peri*-tetracene up to *peri*-heptacene, which have been recently synthesized, display open-shell multiradical features at their ground states. Such open-shell character leads to poor ambient stability and high reactivity, which hampers further studies and applications.[7] For instance, *peri*-tetracene can easily undergo oxidation reactions under ambient conditions, and its bay regions enable its further functionalization through Diels–Alder reactions, yielding the fully zigzag-edged circumanthracene (Figure 1b).[7b,8]

Thus far, two main strategies, sterically blocking the most reactive position (kinetic stabilization) and heteroatom doping (thermodynamic stabilization), have been established to synthesize stable zigzag-edged higher acenes.[3b,9] Specifically, the introduction of heteroatoms such as boron (B) or nitrogen (N) on the zigzag edges, not only provides access to stable heteroatom-doped acenes but also offers the possibility to tune their electronic structures.[3,10] For instance, *bis*-anthene is reactive toward oxygen due to its radicaloid character at its zigzag edges, while B-doped *bis*-anthene is quite stable under ambient conditions and emits intense fluorescence (Figure 1c).[10b,11] Apart from B-doped *bis*-anthene, zwitterionic N-doped dibenzophenalenes (DBPs) also demonstrate higher stability than open-shell DBPs (Figure 1c).[12] In addition to mono- or double B/N-doped zigzag-edged PAHs, recent efforts have been mainly paid to substitute a full C_3 unit at the zigzag edge with an NBN or BNB motif, such as NBN-doped DBPs or BNB-doped phenalenyl (Figure 1c), which possess stable zigzag edges.[13–15] Moreover, owning to the BN/CC isosterism,[14] further oxidation or reduction of these NBN-doped DBPs or BNB-doped phenalenyl generated interesting characteristics, such as comparable electronic structures to their open-shell all-carbon analogs.[13–15] Nonetheless, the multi-NBN-doped zigzag-edged acene-type system remains less explored due to the lack of a suitable molecular design and synthesis strategy.

Herein, we demonstrate the novel synthesis of NBN-doped *bis*-tetracene (**NBN-BT**) and *peri*-tetracene (**NBN-PT**) by combining both in-solution and on-surface synthesis (Figure 1d). First, **NBN-BT** can be achieved via a tandem twofold electrophilic borylation approach based on a tetra(aminophenyl)-phenyl precursor (compound **5** in Scheme 1). Subsequently, **NBN-PT** can be achieved based on **NBN-BT** through in-solution photocyclization (I_2, propylene oxide) and surface-assisted intramolecular cyclodehydrogenation reactions. According to the high-resolution scanning tunneling microscopy (STM) characterization, **NBN-BT** adopts a double-helical structure, while **NBN-PT** displays planar geometry. The chemical structure of **NBN-PT** can be further elucidated by noncontact atomic force microscopy (nc-AFM) at the molecular level. The optical energy gaps of **NBN-BT** and **NBN-PT** are determined to be 2.48 eV and 2.45 eV, respectively, from the onsets of their UV-vis absorption spectra, which are substantially higher than those of their carbon-based analogs *bis*-tetracene (1.56 eV) and *peri*-tetracene (1.11 eV). Interestingly, upon chemical or electrochemical oxidation, **NBN-BT** can be converted into its corresponding radical cation with a near-infrared (NIR) absorption band

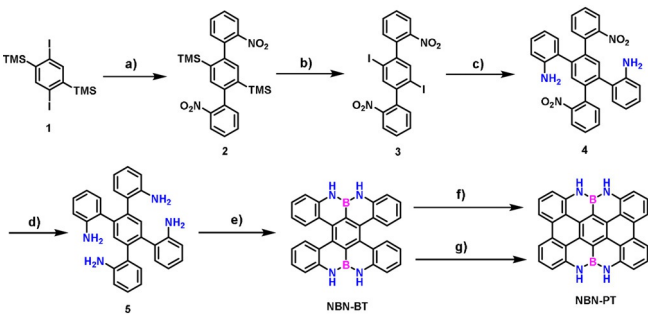

Scheme 1. Synthesis routes toward **NBN-BT** and **NBN-PT**. Reagents and conditions: a) 4,4,5,5-tetramethyl-2-(2-nitrophenyl)-1,3,2-dioxaborolane, Na_2CO_3, DMF, H_2O, $Pd(PPh_3)_4$, 100 °C, 24 h, 78% yield; b) ICl, DCM, 0 °C—r.t., 12 h, 85% yield; c) 2-(4,4,5,5-tetramethyl-1,3,2-dioxaborolan-2-yl)aniline, Na_2CO_3, THF, H_2O, $Pd(dppf)Cl_2$, 70 °C, 24 h, 79% yield; d) H_2, Pt/C, THF/MeOH, r.t., 12 h, 78% yield; e) BI_3, BPh_3, *o*-DCB, 200 °C, 24 h, 20% yield; f) propylene, I_2, toluene, *hν*, r.t., 24 h, trace amount (yield); g) Au(111), 350 °C.

and an electron paramagnetic resonance (EPR) signal, and further oxidized into its dication instead of its diradical dication according to the absent EPR signal. The optical energy gaps of the **NBN-BT** radical cation and dication are derived to be 0.88 eV and 1.24 eV, respectively, the latter being similar to its corresponding isoelectronic structure *bis*-tetracene (1.56 eV). Likewise, DFT calculations reveal a similar energy gap between the **NBN-PT** dication (1.21 eV) and *peri*-tetracene (1.11 eV), demonstrating their isoelectronic relationship.

The synthesis routes toward **NBN-BT** and **NBN-PT** are illustrated in Scheme 1. First, Suzuki coupling was performed between 2,5-diiodo-1,4-di(trimethylsilyl)-phenyl (**1**) and nitrophenyl boronic ester, which provided 2,5-dinitrophenyl-1,4-di(trimethylsilyl)-phenyl (**2**) in 78% yield. By treatment with iodine monochloride (ICl), compound **2** was converted into 2,5-di(nitrophenyl)-1,4-diiodo-phenyl (**3**) in an 85% yield. Subsequently, twofold Suzuki coupling of **3** with aminophenyl boronic ester afforded 2,5-di(nitrophenyl)-1,4-di(aminophenyl)-phenyl (**4**) in a 79% yield. Afterward, compound **4** was reduced in hydrogen gas with Pt/C at room temperature to provide 1,2,4,5-tetra(aminophenyl)-phenyl (**5**) in 78% yield. Finally, **NBN-BT** was successfully achieved in a 20% yield through a tandem twofold electrophilic borylation approach based on compound **5** in the presence of boron triiodide (BI_3), triphenylborane (BPh_3), and dichlorobenzene (*o*-DCB) at 200 °C.[16] To obtain **NBN-PT**, solution-phase synthesis was first performed through a Scholl-type cyclization of **NBN-BT** under 2,3-dichloro-5,6-dicyano-1,4-benzoquinone (DDQ) or iron(III) chloride ($FeCl_3$) condition. However, all attempts failed, probably due to the formation of stable **NBN-BT** radical cation or dication under the oxidative conditions that prevent further cyclization reaction. Nevertheless, **NBN-PT** could be synthesized by a photocyclization reaction of **NBN-BT** in the presence of propylene oxide and iodine (I_2).

The targeted compound **NBN-BT** was purified by silica column chromatography and then precipitated in acetone/n-hexane. **NBN-BT** was first characterized by high-resolution

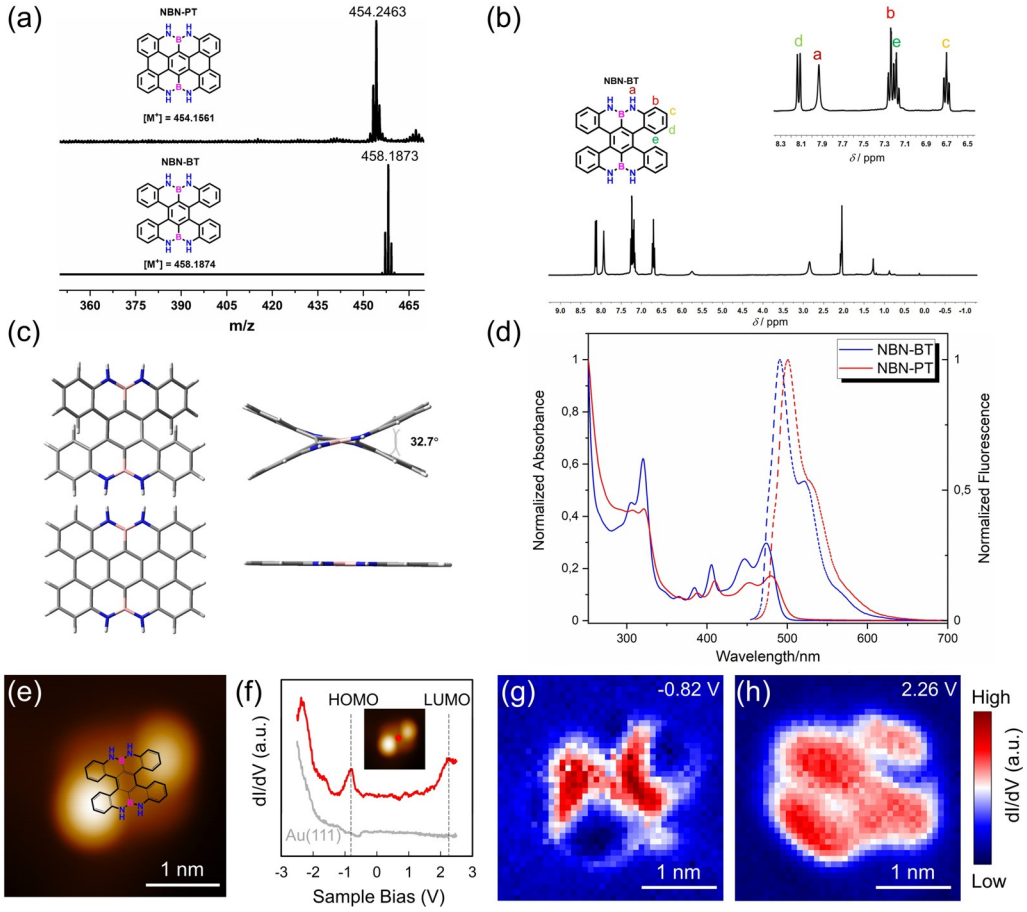

Figure 2. a) MALDI-TOF mass spectra of **NBN-BT** and **NBN-PT**; b) ^{1}H NMR spectrum (300 MHz, 298 K, [D_6]acetone) of **NBN-BT**, inset: assignment for each proton; c) front view (left) and side view (right) of the ground-state optimized structures of **NBN-BT** and **NBN-PT** calculated at the B3LYP-GD3BJ/6-31G(d,p) level; d) UV/Vis absorption (concentration: 1×10^{-5} M) and fluorescence spectra (concentration: 1×10^{-7} M) of **NBN-BT** and **NBN-PT** (crude) in CH_2Cl_2. e) STM topography image of a single **NBN-BT** molecule deposited on Au(111) with the superposed molecular structure. The bright protrusions are benzene rings lifted on the surface; f) differential conductance (dI/dV) spectrum taken of **NBN-BT** (red) and Au(111) (grey); and g,h) dI/dV maps taken at −0.82 V and +2.26 V, respectively, of the same **NBN-BT** molecule in (e). Scanning parameters: (e) $V_s=-1$ V, $I_t=100$ pA; f) $V_s=-2.5$ V, $I_t=300$ pA, $V_{mod}=20$ mV; and (g,h) $I_t=400$ pA, $V_{mod}=10$ mV.

matrix-assisted laser desorption/ionization time of flight mass spectrometry (HR-MALDI-TOF-MS). In Figure 2a, there is only one dominant peak in the mass spectrum of **NBN-BT**, revealing its defined molecular composition; the isotopic distribution pattern of the mass peak is in good agreement with the calculated pattern (Figure S33). The ^{1}H NMR spectrum of **NBN-BT** displays well-resolved peaks (Figure 2b), in which the a-e peaks can be fully assigned by the help of 2D NMR (Figure 2b, and S17–20). In addition, there is one sharp resonance at 20.2 ppm in the ^{11}B NMR spectrum of **NBN-BT** (Figure S16). In contrast to **NBN-BT**, the poor solubility of **NBN-PT** hampers its further purification, leading to its difficult full characterization by NMR and HR-MS. Nonetheless, Figure 2a presents the mass spectrum of **NBN-PT** with the peak center located at 454.2463, which agrees with the calculated molecular weight. In addition, the isotopic distribution pattern of the mass peak fits well with the calculated pattern (Figure S34).

Due to their poor solubility and crystallinity, single-crystal structures of **NBN-BT** and **NBN-PT** cannot be achieved after different crystallization attempts from solvents such as dichloromethane/methanol, acetone/iso-hexane, and tetrahydrofuran/iso-hexane. Through DFT calculations (B3LYP-GD3BJ/6-31G(d,p)), **NBN-BT** shows a double hetero-[5]helicene geometry with a dihedral angle of 32.7° (Figure 2c), while **NBN-PT** exhibits a planar structure. The B–N bond lengths in **NBN-BT** (1.42 Å) and **NBN-PT** (1.43 Å) are much shorter than a typical B–N single bond (1.58 Å) but slightly longer than a localized B=N double bond (1.40 Å).[17] In addition to the DFT-optimized structure, on-surface characterization of **NBN-BT** was performed. According to the high-resolution STM characterizations (Figure 2e), when **NBN-BT** was sublimed onto a Au(111) substrate kept at room temperature under ultrahigh vacuum (UHV) conditions, it demonstrates an "up and down" configuration, clearly revealing a double helical conformation, which is supported by the DFT calculations (Figure 2c). The differential conductance (dI/dV) spectrum in Figure 2f displays that the HOMO and LUMO energy levels locate at −0.82 V and +2.26 V, respectively, which gives an energy gap of 3.08 eV for **NBN-BT**, comparable with the DFT calculation results (3.07 eV, Figure S25). The dI/dV maps at the HOMO and

LUMO energy levels of **NBN-BT** are shown in Figure 2g and 2h, respectively, in which the HOMO is mainly located at the planar part of **NBN-BT**, while the LUMO is delocalized over the entire molecule.

The UV-vis absorption and fluorescence spectra of **NBN-BT** and the crude product of **NBN-PT** in anhydrous dichloromethane (DCM) solution are presented in Figure 2d. Due to the rigid conjugated structure of **NBN-BT**, well-resolved vibronic bands are observed. In particular, the maximum absorption peak at 474 nm can be assigned to the HOMO→LUMO transition based on time-dependent density functional theory (TD-DFT) calculations (Figure S29). The optical energy gap of **NBN-BT** is estimated to be 2.48 eV from the UV-vis absorption edge (Figure 2d), which is substantially larger than that of the fully carbon-based analog *bis*-tetracene (1.56 eV).[7a] In contrast to the nonfluorescent *bis*-tetracene, **NBN-BT** exhibits intense yellow-green fluorescence (quantum yield: 0.31, using fluorescein as the reference) with a maximum emission peak at 491 nm (Figure 2d). Accordingly, the Stokes shift is as small as 17 nm, manifesting the rigid conjugated structure of **NBN-BT**. Regarding the crude product of **NBN-PT**, its maximum absorption peak (480 nm) is slightly redshifted compared with that of **NBN-BT** (474 nm), indicating the extended π-conjugated structures of **NBN-BT** over **NBN-PT**. Moreover, the maximum emission peak of **NBN-PT** (501 nm) is redshifted compared to that of **NBN-BT** (491 nm).

The electrochemical behavior of compound **NBN-BT** in anhydrous acetonitrile (MeCN) was further investigated by means of cyclic voltammetry (CV) measurements (Figure S22). Two oxidation processes are observed with half-wave potentials of 0.23 and 0.47 V vs. Fc^+/Fc, respectively. Nevertheless, no reduction process is observed. Accordingly, the HOMO energy level of **NBN-BT** is estimated to be −4.57 eV (Table S1). On the basis of its optical energy gap, the LUMO energy level of **NBN-BT** is derived to be −2.09 eV (Table S1). The HOMO energy level of **NBN-BT** is comparable to that of all-carbon-based *bis*-tetracene, while the LUMO energy level is obviously higher than that of *bis*-tetracene (Table S1). The CV measurement of **NBN-PT** cannot be performed due to its poor solubility. Nonetheless, DFT calculations based on **NBN-PT** reveal its HOMO (−4.68 eV) and LUMO (−1.31 eV) energy level, as well as energy gap (3.37 eV), in contrast to those of the all-carbon-based *peri*-tetracene (HOMO/LUMO/energy gap: −4.38/−2.62/1.76 eV, Table S1). Therefore, the different electronic properties and stabilities of **NBN-BT** and **NBN-PT** from *bis*-tetracene and *peri*-tetracene can be attributed to the unique NBN dopant units at the zigzag edges.

In addition to the solution synthesis of **NBN-PT**, we further carried out the on-surface synthesis of **NBN-PT** from the precursor **NBN-BT**. Planarized **NBN-PT** was achieved by thermal annealing **NBN-BT** on Au(111) at 350 °C. Figure 3a,b present the STM image in which the **NBN-PT** molecules separately appear on the Au(111) substrate. To unambiguously clarify the atomically resolved structure of **NBN-PT**, nc-AFM measurements with a CO-functionalized tip were performed. Figure 3c depicts the resulting constant-height frequency-shift image in which each atom and bond of **NBN-PT** can be clearly visualized. The d*I*/d*V* spectra in Figure 3d reveal the HOMO and LUMO energy levels of **NBN-PT** to be −0.88 eV and 2.40 eV, respectively. Accordingly, the corresponding energy gap is 3.28 eV, which is further supported by DFT calculations (Figure S25, 3.37 eV). Compared to the optical energy gaps of **NBN-BT** (2.48 eV) and **NBN-PT** (2.45 eV), the STS measured energy gaps of **NBN-BT** (3.08 eV) and **NBN-PT** (3.28 eV) are clearly higher, which can be attributed to their strong interaction with the Au substrate.[18] Moreover, planarized **NBN-PT** can have a stronger interaction with the Au substrate than the nonplanarized **NBN-BT**, which leads to larger energy gap change of **NBN-PT**.[18] The d*I*/d*V* map at a HOMO energy of −0.88 eV in Figure 3e shows that the armchair edges of **NBN-PT** have much stronger intensity than the rest of the molecule. On the other hand, regarding the d*I*/d*V* map at the LUMO energy (2.40 eV) in Figure 3f, both the armchair and zigzag edges possess a stronger state than that at the center of the molecule. Besides, the existence of NBN dopants slightly weaken the HOMO state intensity than that at the carbon periphery, as indicated by the yellow arrows in Figure 3f.

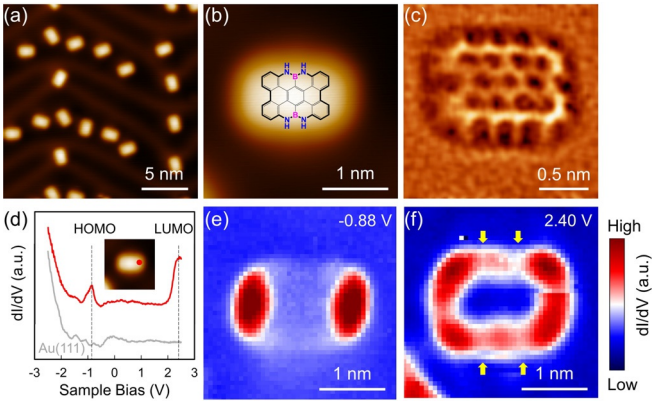

Figure 3. a) STM topography image of **NBN-PT** molecules; b) STM topography image of one single **NBN-PT** molecule with the superposed molecular structure; c) constant-height frequency-shift nc-AFM image of one **NBN-PT** on Au(111) after Laplace filtering; d) d*I*/d*V* spectrum of **NBN-PT** (red) and Au(111) (grey); and e,f) d*I*/d*V* maps taken at −0.88 V and +2.40 V, respectively, of the same **NBN-PT** molecule in (b). The yellow arrows in (f) indicate the positions of N atoms. Scanning parameters: (a,b) $V_s = -1$ V, $I_t = 50$ pA; (d) amplitude = 100 pm; d) $V_s = -2.5$ V, $I_t = 800$ pA, $V_{mod} = 20$ mV; and (e,f) $I_t = 800$ pA, $V_{mod} = 10$ mV.

The NBN unit not only provides the high stability of **NBN-BT** but can also be further subjected to oxidation into the corresponding radical cation and dication, which provides the chemical tunability of NBN-doped zigzag-edged PAHs.[13a] Toward this end, the chemical oxidation of **NBN-BT** was carried out by using $Cu(OTf)_2$. Indeed, the titration of **NBN-BT** with $Cu(OTf)_2$ results in a mega-large (800 nm) bathochromic shift of the UV-vis absorption bands (Figure 4a). During the progressive addition of $Cu(OTf)_2$ from 0 to 1.0 equivalents, a series of new absorption peaks in the visible and NIR regions gradually appear at 684 and 1239 nm with a concomitant decrease in the absorption bands at 320 and 476 nm. In addition, a distinct isosbestic point at 500 nm can be observed (Figure 4a). The strong NIR absorption band in

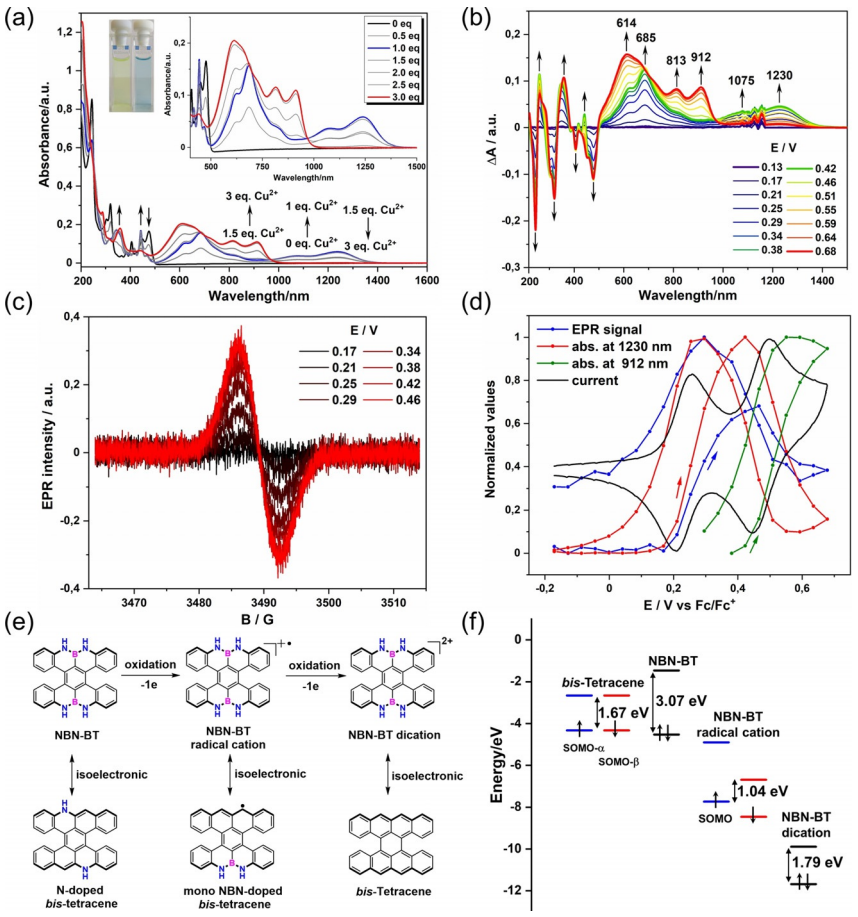

Figure 4. a) UV/Vis/NIR absorption spectra of **NBN-BT** titrated with $Cu(OTf)_2$ (0, 0.5, 1.0, 1.5, 2.0, 2.5, 3.0 equivalents) at a concentration of 10^{-5} M in MeCN (reference spectrum: MeCN solution), inset: photographs of the **NBN-BT** and **NBN-BT** radical cation/dication in MeCN; b) UV/Vis/NIR spectra measured during the electrochemical oxidation of **NBN-BT** in MeCN solution (reference spectrum: **NBN-BT** solution); c) EPR spectra of **NBN-BT** recorded in situ at different potentials; d) the potential profiles of absorption bands and the EPR signal intensity (only the representative bands at 1230 and 912 nm are presented); e) the plausible oxidation process of **NBN-BT** and its corresponding isoelectronic structures; f) Calculated energy diagrams and energy gaps of *bis*-tetracene, **NBN-BT**, **NBN-BT** radical cation and **NBN-BT** dication (SOMO: single occupied molecular orbital).

the range of 900–1400 nm indicates the formation of the **NBN-BT** radical cation. With the addition of $Cu(OTf)_2$ from 1.5 to 3.0 equivalents, the absorption peak in the NIR region at 1239 nm gradually vanishes with a concomitant evolution of three new absorption peaks at 609, 816, and 912 nm. After the addition of more than 3.0 equivalents of $Cu(OTf)_2$, the UV-vis-NIR absorption spectra remains unchanged, indicating that no more chemical oxidation processes occur. Moreover, an extremely rapid and well-defined change from a light-yellow solution in the neutral state to a light-cyan solution in the radical cation/dication state is observed by the naked eye (Figure 4a insert).

According to the CV results, **NBN-BT** can undergo two reversible oxidation processes. In the first step, **NBN-BT** loses one electron to form the **NBN-BT** monoradical cation ($[\mathbf{NBN\text{-}BT}]^{+\bullet}$, Figure 4e), which possesses an open-shell character. After adding more than 1.0 equivalent of $Cu(OTf)_2$, the second oxidation step occurs, and a possible product can be the **NBN-BT** diradical dication ($[\mathbf{NBN\text{-}BT}]^{2+\bullet\bullet}$) or **NBN-BT** dication ($[\mathbf{NBN\text{-}BT}]^{2+}$, Figure 4e), which can be regarded as the isoelectronic structures of all-carbon-based *bis*-tetracene (Figure 4e). To determine the reaction species formed during the chemical oxidation process of **NBN-BT**, in situ spectroelectrochemical (SEC) measurements, a combination of CV, electron paramagnetic resonance (EPR) and UV-vis-NIR absorption spectroscopy, were performed. The EPR spectra show a broad unresolved signal with a *g* value of 2.0027 during the first oxidation process in the CV curve (Figure 4c). The appearance of a broad signal without hyperfine splitting (see Figure S23) reveals that the spin density in $[\mathbf{NBN\text{-}BT}]^{+\bullet}$ is distributed over the whole molecular skeleton. The UV-vis-NIR spectra of the charged species generated during the chemical and electrochemical oxidation of **NBN-BT** are identical (Figure 4a and b). Additionally, the absorption bands and the ESR signal appear simultaneously, and their intensities show the same potential profile (Figure 4d). These absorption bands can be unambiguously attributed to the corresponding monoradical species $[\mathbf{NBN\text{-}BT}]^{+\bullet}$. At the potentials of the second oxidation process in CV, the intensities of the ESR signal and absorption bands of the radical cation (1230 nm as representative band) decrease, and new absorption bands (912 nm as representative band) occur in the UV-vis-NIR spectra (Figure 4d), suggesting that $[\mathbf{NBN\text{-}BT}]^{+\bullet}$ converts into the diamagnetic species $[\mathbf{NBN\text{-}BT}]^{2+}$ instead of the diradical dication $[\mathbf{NBN\text{-}BT}]^{2+\bullet\bullet}$. Based on the UV-vis absorption edge, the optical energy gaps of $[\mathbf{NBN\text{-}BT}]^{+\bullet}$ and $[\mathbf{NBN\text{-}BT}]^{2+}$ are estimated to be 0.88 eV and 1.24 eV, respectively. Compared to the optical energy gap of *bis*-tetracene (1.56 eV),[7a] $[\mathbf{NBN\text{-}BT}]^{2+}$ displays a comparable energy gap, suggesting their isoelectronic relationship (Figure 4e). To gain deeper insight into the chemical oxidation process of **NBN-BT**, DFT calculations were further performed. As shown in Figure 4f, after the first single-electron oxidation of **NBN-BT**, the energy gap of $[\mathbf{NBN\text{-}BT}]^{+\bullet}$ decreases to 1.04 eV. Furthermore, the spin distribution of $[\mathbf{NBN\text{-}BT}]^{+\bullet}$ is highly delocalized (Figure S27), demonstrating its π-conjugated structure. After the second single-electron oxidation, the energy gap of $[\mathbf{NBN\text{-}BT}]^{2+}$ increases to 1.79 eV, which is comparable to that of the calculated pristine carbon analog *bis*-tetracene (1.67 eV in Figure 4f).

On the other hand, it is difficult to perform titration experiments for **NBN-PT** due to its poor solubility. Therefore,

DFT calculations of **NBN-PT** are employed to study its corresponding oxidation behavior. Likewise, the energy gaps of the **NBN-PT** radical cation ([**NBN-PT**]$^{+\bullet}$, 0.96 eV) and dication ([**NBN-PT**]$^{2+}$, 1.21 eV) are significantly lower than that of its neutral compound (3.37 eV, Figure S28). Similar to **NBN-BT**, [**NBN-PT**]$^{2+}$ exhibits a calculated energy gap similar to that of *peri*-tetracene (1.76 eV, Figure S28), which clearly reveals their isoelectronic relationship (Figure S28).

In summary, we demonstrated the novel synthesis of two double NBN-doped zigzag-edged nanographenes, namely, *bis*-tetracene (**NBN-BT**) and *peri*-tetracene (**NBN-PT**), through a combination of solution-based and surface-assisted synthesis. Based on the high-resolution STM characterization, **NBN-BT** adopts a double-helical structure, while **NBN-PT** displays planar geometry, in which the atomically resolved structure of **NBN-PT** is further unveiled by nc-AFM characterization. Compared with their carbon-based analogs *bis*-tetracene (1.56 eV) and *peri*-tetracene (1.11 eV), the **NBN-BT** (2.48 eV) and **NBN-PT** (2.45 eV) exhibit excellent stability under ambient conditions, which is associated with their higher energy gap. Notably, through controlled continuous single-electron chemical or electrochemical oxidation, **NBN-BT** can be converted into its corresponding radical cation (0.88 eV) and further to dication (1.24 eV), which demonstrates a similar energy gap to its isoelectronic structure *bis*-tetracene (1.56 eV). This work opens up a new avenue for the synthesis of stable zigzag-edged nanographenes with multi-NBN units and paves the way for investigating the isoelectronic structures of pristine carbon-based zigzag-edged acenes.

Acknowledgements

This work was supported by the European Union's Horizon 2020 (No 881603 Graphene Flagship Core3, No 813036 Marie Skłodowska-Curie), ERC Grant on T2DCP, German DFG (Cluster of Excellence "Center for Advancing Electronics Dresden (cfaed) and DFG-NSFC Joint Sino-German Research Project (EnhanceNano, No. 391979941), as well as the DFG-SNSF Joint Switzerland-German Research Project (EnhanTopo, No. 429265950). J. Liu is grateful for the funding support from the Hong Kong Research Grants Council (HKU 27301720) and ITC to the SKL. We thank the National Natural Science Foundation of China (Grant Nos. 61888102, and 61674045), the Ministry of Science and Technology (MOST) of China (No. 2019YFA0308500), as well as the Strategic Priority Research Program of Chinese Academy of Sciences (Grant Nos. XDB30000000). We thank the Center for Information Services and High Performance Computing (ZIH) at TU Dresden for generous allocations of compute resources. Open Access funding enabled and organized by Projekt DEAL.

Conflict of Interest

The authors declare no conflict of interest.

Keywords: *bis*-tetracene · isoelectronic · NBN doping · *peri*-tetracene · zigzag edges

[1] a) J. E. Anthony, *Angew. Chem. Int. Ed.* **2008**, *47*, 452 – 483; *Angew. Chem.* **2008**, *120*, 460 – 492; b) M. Bendikov, F. Wudl, D. F. Perepichka, *Chem. Rev.* **2004**, *104*, 4891 – 4946; c) S. S. Zade, M. Bendikov, *J. Phys. Org. Chem.* **2012**, *25*, 452 – 461; d) R. A. Pascal, *Chem. Rev.* **2006**, *106*, 4809 – 4819; e) M. Pinheiro, L. F. A. Ferrão, F. Bettanin, A. J. A. Aquino, F. B. C. Machado, H. Lischka, *Phys. Chem. Chem. Phys.* **2017**, *19*, 19225 – 19233; f) W. Chen, F. Yu, Q. Xu, G. Zhou, Q. Zhang, *Adv. Sci.* **2020**, *7*, 1903766; g) D.-e. Jiang, S. Dai, *J. Phys. Chem. A* **2008**, *112*, 332 – 335.

[2] a) Z. Sun, Z. Zeng, J. Wu, *Acc. Chem. Res.* **2014**, *47*, 2582 – 2591; b) Z. Sun, Q. Ye, C. Chi, J. Wu, *Chem. Soc. Rev.* **2012**, *41*, 7857 – 7889; c) K. Sbargoud, M. Mamada, T. Jousselin-Oba, Y. Takeda, S. Tokito, A. Yassar, J. Marrot, M. Frigoli, *Chem. Eur. J.* **2017**, *23*, 5076 – 5080; d) Y. Gu, Y. G. Tullimilli, J. Feng, H. Phan, W. Zeng, J. Wu, *Chem. Commun.* **2019**, *55*, 5567 – 5570; e) J.-J. Shen, Y. Han, S. Dong, H. Phan, T. S. Herng, T. Xu, J. Ding, C. Chi, *Angew. Chem. Int. Ed.* **2021**, *60*, 4464 – 4469; *Angew. Chem.* **2021**, *133*, 4514 – 4519.

[3] a) J. Liu, X. Feng, *Angew. Chem. Int. Ed.* **2020**, *59*, 23386 – 23401; *Angew. Chem.* **2020**, *132*, 23591 – 23607; b) J. Liu, R. Berger, K. Müllen, X. Feng in *From Polyphenylenes to Nanographenes and Graphene Nanoribbons* (Eds.: K. Müllen, X. Feng), Springer International Publishing, Cham, **2017**, pp. 1 – 32.

[4] D. Lungerich, O. Papaianina, M. Feofanov, J. Liu, M. Devarajulu, S. I. Troyanov, S. Maier, K. Amsharov, *Nat. Commun.* **2018**, *9*, 4756.

[5] S. Das, J. Wu, *Polycyclic Arenes and Heteroarenes*, Wiley-VCH, Hoboken, **2015**, pp. 1 – 36.

[6] a) R. Scholl, J. Mansfeld, *Ber. Dtsch. Chem. Ges.* **1910**, *43*, 1734 – 1746; b) E. Clar, *Chem. Ber.* **1948**, *81*, 52 – 63.

[7] a) J. Liu, P. Ravat, M. Wagner, M. Baumgarten, X. Feng, K. Müllen, *Angew. Chem. Int. Ed.* **2015**, *54*, 12442 – 12446; *Angew. Chem.* **2015**, *127*, 12619 – 12623; b) M. R. Ajayakumar, Y. Fu, J. Ma, F. Hennersdorf, H. Komber, J. J. Weigand, A. Alfonsov, A. A. Popov, R. Berger, J. Liu, K. Müllen, X. Feng, *J. Am. Chem. Soc.* **2018**, *140*, 6240 – 6244; c) Y. Ni, T. Y. Gopalakrishna, H. Phan, T. S. Herng, S. Wu, Y. Han, J. Ding, J. Wu, *Angew. Chem. Int. Ed.* **2018**, *57*, 9697 – 9701; *Angew. Chem.* **2018**, *130*, 9845 – 9849; d) S. Mishra, T. G. Lohr, C. A. Pignedoli, J. Liu, R. Berger, J. I. Urgel, K. Müllen, X. Feng, P. Ruffieux, R. Fasel, *ACS Nano* **2018**, *12*, 11917 – 11927; e) C. Rogers, C. Chen, Z. Pedramrazi, A. A. Omrani, H.-Z. Tsai, H. S. Jung, S. Lin, M. F. Crommie, F. R. Fischer, *Angew. Chem. Int. Ed.* **2015**, *54*, 15143 – 15146; *Angew. Chem.* **2015**, *127*, 15358 – 15361; f) M. R. Ajayakumar, J. Ma, A. Lucotti, K. S. Schellhammer, G. Serra, E. Dmitrieva, M. Rosenkranz, H. Komber, J. Liu, F. Ortmann, M. Tommasini, X. Feng, *Angew. Chem. Int. Ed.* **2021**, *60*, 13853 – 13858; *Angew. Chem.* **2021**, *133*, 13972 – 13977.

[8] M. R. Ajayakumar, Y. Fu, F. Liu, H. Komber, V. Tkachova, C. Xu, S. Zhou, A. A. Popov, J. Liu, X. Feng, *Chem. Eur. J.* **2020**, *26*, 7497 – 7503.

[9] a) M. Müller, L. Ahrens, V. Brosius, J. Freudenberg, U. H. F. Bunz, *J. Mater. Chem. C* **2019**, *7*, 14011 – 14034; b) C.-I. Chia, V. H. Crespi, *Phys. Rev. Lett.* **2012**, *109*, 076802.

[10] a) J. Liu, X. Feng, *Synlett* **2020**, *31*, 211 – 222; b) V. M. Hertz, M. Bolte, H.-W. Lerner, M. Wagner, *Angew. Chem. Int. Ed.* **2015**, *54*, 8800 – 8804; *Angew. Chem.* **2015**, *127*, 8924 – 8928.

[11] S. M. Arabei, T. A. Pavich, *J. Appl. Spectrosc.* **2000**, *67*, 236 – 244.

[12] R. Berger, A. Giannakopoulos, P. Ravat, M. Wagner, D. Beljonne, X. Feng, K. Müllen, *Angew. Chem. Int. Ed.* **2014**, *53*, 10520 – 10524; *Angew. Chem.* **2014**, *126*, 10688 – 10692.

[13] a) X. Wang, F. Zhang, K. S. Schellhammer, P. Machata, F. Ortmann, G. Cuniberti, Y. Fu, J. Hunger, R. Tang, A. A. Popov, R. Berger, K. Müllen, X. Feng, *J. Am. Chem. Soc.* **2016**, *138*, 11606 – 11615; b) H. Wei, Y. Liu, T. Y. Gopalakrishna, H. Phan, X. Huang, L. Bao, J. Guo, J. Zhou, S. Luo, J. Wu, Z. Zeng, *J. Am. Chem. Soc.* **2017**, *139*, 15760 – 15767.

[14] a) X.-Y. Wang, J.-Y. Wang, J. Pei, *Chem. Eur. J.* **2015**, *21*, 3528 – 3539; b) P. G. Campbell, A. J. V. Marwitz, S.-Y. Liu, *Angew. Chem. Int. Ed.* **2012**, *51*, 6074 – 6092; *Angew. Chem.* **2012**, *124*, 6178 – 6197; c) C. R. McConnell, S.-Y. Liu, *Chem. Soc. Rev.* **2019**, *48*, 3436 – 3453.

[15] Y. Fu, H. Yang, Y. Gao, L. Huang, R. Berger, J. Liu, H. Lu, Z. Cheng, S. Du, H.-J. Gao, X. Feng, *Angew. Chem. Int. Ed.* **2020**, *59*, 8873 – 8879; *Angew. Chem.* **2020**, *132*, 8958 – 8964.

[16] K. Matsui, S. Oda, K. Yoshiura, K. Nakajima, N. Yasuda, T. Hatakeyama, *J. Am. Chem. Soc.* **2018**, *140*, 1195 – 1198.

[17] Y. Fu, K. Zhang, E. Dmitrieva, F. Liu, J. Ma, J. J. Weigand, A. A. Popov, R. Berger, W. Pisula, J. Liu, X. Feng, *Org. Lett.* **2019**, *21*, 1354 – 1358.

[18] a) N. Merino-Díez, A. Garcia-Lekue, E. Carbonell-Sanromà, J. Li, M. Corso, L. Colazzo, F. Sedona, D. Sánchez-Portal, J. I. Pascual, D. G. de Oteyza, *ACS Nano* **2017**, *11*, 11661 – 11668; b) O. Deniz, C. Sánchez-Sánchez, T. Dumslaff, X. Feng, A. Narita, K. Müllen, N. Kharche, V. Meunier, R. Fasel, P. Ruffieux, *Nano Lett.* **2017**, *17*, 2197 – 2203; c) M. Shekhirev, P. Zahl, A. Sinitskii, *ACS Nano* **2018**, *12*, 8662 – 8669; d) K. Xu, J. I. Urgel, K. Eimre, M. Di Giovannantonio, A. Keerthi, H. Komber, S. Wang, A. Narita, R. Berger, P. Ruffieux, C. A. Pignedoli, J. Liu, K. Müllen, R. Fasel, X. Feng, *J. Am. Chem. Soc.* **2019**, *141*, 7726 – 7730.

Manuscript received: July 22, 2021
Revised manuscript received: September 12, 2021
Accepted manuscript online: September 14, 2021
Version of record online: November 5, 2021

